A Simple Head-sized Phantom for Realistic Static and Radiofrequency Characterization at High Fields

W.M. Brink, Z. Wu, and A.G. Webb

C.J. Gorter Center for High Field MRI, Department of Radiology

Leiden University Medical Center, Leiden, The Netherlands.

Corresponding author:

A.G. Webb,

C.J.Gorter Center for High Field MRI,

Department of Radiology, Postzone C3-Q,

Leiden University Medical Center,

Albinusdreef 2, 2333 ZA,

Leiden, The Netherlands.

Telephone: +31-71-526-5483

Fax: +31-71-524-8256

Email: a.webb@lumc.nl

Word count: 2916

Running title: A Simple Head Phantom for High Field MRI

Key words: High Field MRI, head phantom, B_0 and B_1^+ nonuniformity, MR Thermometry

Abstract

Purpose: To demonstrate a simple head-sized phantom for realistic static and radiofrequency field characterization in high field systems.

Methods: The head-sized phantom was composed of an ellipsoidal compartment and a spherical cavity to mimic the nasal cavity. The phantom was filled with an aqueous solution of polyvinylpyrrolidone (PVP), to mimic the average dielectric properties of brain tissue. The static and radiofrequency (RF) field distributions were characterized on a 7T MRI system and compared to in vivo measurements and simulations. MR thermometry was performed and the results were compared to thermal simulations for RF validation purposes.

Results: Accurate reproduction of both static and RF fields patterns observed in vivo was confirmed experimentally, and was shown to be strongly affected by the inclusion of the spherical cavity. MR thermometry and transmit efficiency (B_1^+) measurements were obtained in close agreement with simulations (peak values agreeing within 0.3 °C and 0.02 μT/√W) as well as fiber optic thermal probes (RMSE < 0.18 °C).

Conclusions: A simple head-sized phantom has been presented which produces B_0 and B_1^+ nonuniformities similar to those encountered in the human head, and allows for accurate MR thermometry measurements, making this a suitable reference phantom for RF validation and methodological development in high field MRI.

Introduction

Tissue-mimicking magnetic resonance (MR) phantoms are instrumental for various MR applications including sequence development as well as system characterization and quality assurance. Tissue properties that are often mimicked include MR relaxation times such as T1 and T2 (1,2), magnetic susceptibility (3), diffusive properties (4), flow (5) and dielectric properties (6). Dosimetric phantoms are also commonly used as reference standards for radiofrequency (RF) safety assessment of implants at 1.5 and 3 Tesla (T) (7).

As MR systems continue to increase in static field strength, with whole body systems reaching 10.5T (8), the associated increases in RF frequency lead to a much stronger load-dependence of the RF fields involved (9,10). Inhomogeneities in the transmit RF (B_1^+) field are generally governed by the bulk dielectric properties of the sample, leading to a shortening of the RF wavelength, as well as being sensitive to the geometry and positioning of the sample (6,11). In the head at 7T, these B_1^+ field patterns involve pronounced areas of low transmit efficiency in the temporal lobes, which can be attributed to the elliptical shape of the head (11). Additionally, local dielectric heterogeneities in the sample can lead to local B_1^+ perturbations (12), but more importantly, can confine the local RF power deposition and corresponding specific absorption rate (SAR) (13–15). RF safety analyses therefore generally involve heterogeneous body models with many different tissue types to capture such mechanisms and determine safe power limits at which MR systems can be operated.

An important step in such RF safety assessments is to validate the simulated coil model via RF field mapping and MR thermometry techniques, guided by a well-defined reference phantom (16). The increased load-dependence at high field strengths underlines the importance of performing such a validation under realistic loading conditions, so that the validation corresponds well with the in vivo situation. This aspect will become more relevant as MR systems are moving from single channel transmission using a volume coil towards parallel transmission using transmit arrays composed of surface elements (17), which are more dependent on inter-element coupling and generally more complex to model. A phantom which produces realistic B_1^+ non-uniformities would also be valuable in the development of MR methods for RF inhomogeneity correction such as multidimensional RF pulses, dielectric shimming or parallel transmission (17–19).

Given such considerations, there is a growing interest in head-mimicking phantoms with increasing complexity to reproduce these sensitivities in a realistic manner (20–23). Several materials such as aqueous solutions of polyethylene powder (21,24), sugar (22,25) or ethanol (23) are known to allow

for appropriate tuning of their dielectric properties to reach values similar to those of human tissues. These phantom recipes typically incorporate salt as an additive to control electrical conductivity and also gelling agents to reduce thermal convection (26). Advanced 3D-printed anthropomorphic phantoms with multiple compartments have also been proposed to better reproduce the dielectric heterogeneity of the human head (21,23). Despite these efforts, the correspondence of the RF fields obtained in these advanced phantom designs with those obtained in vivo is still rather weak.

In the current work, we present a very simple head-sized phantom composed of a single ellipsoidal compartment and a spherical air cavity to mimic the nasal cavity. It is filled with an aqueous solution of polyvinylpyrrolidone (PVP), which has recently been shown to feature advantageous properties such as a high signal-to-noise ratio (SNR) and low spectral contamination with respect to conventional phantom materials (27). Experiments performed at 7T show that the phantom produces both static (B_0) and RF transmit (B_1^+) field interactions corresponding very closely to those produced in the head in vivo. The phantom was also tested in terms of the measured temperature rise when using a high permittivity dielectric pad and compared to thermal simulations and fiber optic probe readings.

Methods

Phantom design

The head-sized phantom was designed by means of electromagnetic simulations (XFdtd 7.5, Remcom inc., State College, USA). The geometry of the phantom was designed to approximate the head contours of the heterogeneous body model 'Duke' of the Virtual Family (28), which resulted in an ellipsoidal structure of 18×22×27 cm in size as shown in Figure 1. The dielectric properties of the phantom were then optimized in steps of 5 in relative permittivity (ε_r) and in steps of 0.05 S/m in electrical conductivity (σ) in order to reproduce the B_1^+ field patterns produced in the heterogeneous head model when positioned in a numerical model of the birdcage transmit coil. This resulted in a relative permittivity of $\varepsilon_r = 50$ and electrical conductivity of $\sigma = 0.6$ S/m, which is very similar to the average dielectric properties of brain tissue (estimated by averaging the properties of grey and white matter) yielding $\varepsilon_r = 52$ and $\sigma = 0.55$ S/m (29). Finally, a 7-cm diameter spherical cavity was incorporated at an offset of 6 cm from the phantom center in the anterior-posterior direction to account for both the static (B_0) and the RF transmit (B_1^+) field perturbations induced by the nasal cavity (30).

The ellipsoidal phantom shell (Simulacrum Capitis, VDL Wientjes-Roden B.V., Roden, The Netherlands) was constructed from polymethylmethacrylate (PMMA). Two hemispherical shells were constructed using a vacuum-forming technique, and connected to an elliptical ring which was created by means of computer numerical controlled milling. The spherical cavity was implemented using a hollow PMMA sphere, supported by a thin PMMA bar running in the anterior-posterior direction within the central ring. The shell was filled using an aqueous solution of 76g polyvinylpyrrolidone (PVP10, Sigma Aldrich, The Netherlands) with 1.78g Sodium Chloride (NaCl) per 100g of demineralized water, in order to reach the desired dielectric properties (27). We note that the recipe of this solution differs from the recipe reported in (27) due to the difference in polymer chain length of the polyvinylpyrrolidone compound (31). The solution was finally gelled using 1.5% (w/w) agarose (A9539, Sigma Aldrich, The Netherlands) to reduce thermal convection.

The dielectric properties of the phantom material were characterized using a dielectric probe kit (DAK-12, SPEAG, Zürich, Switzerland) at a relative permittivity of $\varepsilon_r = 50.1$ and electrical conductivity of $\sigma = 0.58$ S/m. The thermodynamic properties were determined using a thermal probe (KD2-PRO, Decagon Devices, Pullman, USA) at a thermal conductivity of 0.404 W/(m·K) and volumetric heat capacity of 3.430 MJ/(m^3·K). The volumetric mass density was measured to be 1050 kg/m^3. Despite not being intentionally optimized, these thermodynamic properties show a good agreement with average literature values of grey and white matter, which yield a thermal conductivity of 0.51 W/(m·K), a volumetric heat capacity of 3.797 MJ/(m^3·K) and a density of 1043 kg/m^3 (32).

MR System and RF Coil

All experiments were performed on a whole body 7T MR system operating at an RF frequency of 298 MHz (Achieva, Philips Healthcare, Best, the Netherlands). B_0 and B_1^+ field characterization in the phantom and comparisons with that obtained in vivo were performed using a commercial quadrature birdcage transceive coil with 32-channel receive array (Nova Medical, Wilmington, MA). MR thermometry was performed using a custom-built quadrature birdcage RF coil so that all circuit elements could be modeled exactly (some features of the commercial coil are restricted in their description by the manufacturer). The custom birdcage had an inner diameter of 30 cm, 16 rungs with a length of 17 cm and a shield with a diameter of 36 cm. The birdcage structure was of a high-pass design and was tuned to resonate in the homogeneous mode using fixed end-ring capacitances of 7.1 pF. The two orthogonal ports of the coil were connected between the end ring and the shield to improve coil balance (33). The in vivo study protocol was approved by the local institutional review board and informed consent was obtained.

Static and RF Field Mapping

B_0 and B_1^+ field maps obtained in the phantom were compared with in vivo data obtained in a male volunteer using the commercial RF coil setup, and with B_1^+ simulations when using the custom-built birdcage coil. B_1^+ maps were acquired using a multi-slice DREAM sequence (2.5 mm^2 in-plane resolution, 5 mm slice thickness, TR/TE = 3.2/1.1 ms, STEAM/imaging tip angle = 50°/10°), and normalized with respect to the input power accepted by the coil. B_0 maps were acquired using a dual-echo gradient echo sequence (3.75 mm^3 isotropic resolution, 240 mm^3 field-of-view, TR/TE/ΔTE = 4.0/1.55/1.0 ms, tip angle = 10°). All receive array reconstructions were performed via a Roemer reconstruction (34).

MR thermometry

The second part of this study evaluates the utility of the phantom for MR thermometry using the custom birdcage coil. MR thermometry was performed via the proton resonance frequency (PRF) shift method (35), using a dynamic series of 3D gradient echo acquisitions (3.75 mm^3 isotropic resolution, FOV = 240 mm^3, TR/TE = 15/10 ms, acquisition time = 60 s per dynamic, 30 dynamics) with a total duration of 30 minutes. The TE was chosen as a compromise between the PRF-optimal T_2^* (27 ms) of the phantom material (36), and a shorter TE which reduces the degree of signal loss caused by the static field inhomogeneities within the phantom. A preparation module was added using a block-pulse modulated 100 kHz off-resonance to raise the time-averaged RF power deposition of the sequence without interfering with the image acquisition process. The SAR limits of the system were raised during the heating experiment in order to allow for increasing the RF power deposition of the sequence.

Temperature difference maps were reconstructed from the phase difference with respect to the first dynamic, according to

$$\Delta T = \frac{\Delta\varphi}{\alpha\gamma B_0 TE}$$

in which ΔT is the temperature difference, $\Delta\varphi$ is the phase difference and γ the gyromagnetic ratio. The PRF coefficient (α) relating temperature to phase change was determined to be the same as that of water (α = -0.01 ppm/°C) in a separate cooling experiment (data not shown). Temporal phase unwrapping was performed for each voxel. Mineral oil phantoms were included in the setup to perform bias field correction up to first order (i.e. both constant and spatial gradient terms) by means of a least squares fitting procedure (35). Two fiber optic temperature probes (OTG-MPK5 series, Opsens, Quebec City, CA) were inserted into the phantom to validate the reconstructed temperature maps. A separate 3D gradient echo acquisition at 1.5 mm^3 isotropic resolution was used to locate the probe tips.

The transmitted RF power was measured at the coil plugs to be 51.1 W using a calibrated RF power meter (PSM 5320, Tektronix Inc., Beaverton, OR). The input reflection coefficients of the loaded birdcage coil (S_{11} and S_{22}) were measured at -11.9 dB and -11.2 dB via a network analyzer (TR1300/1, Copper Mountain Technologies, Indianapolis, IN), which resulted in a total of 47.5 W of RF power entering the coil. Thermal simulations were performed in XFdtd (XFdtd 7.5, Remcom inc., State Collega, PA) using these parameters to model the corresponding temperature increase.

Additionally, the RF heating experiment was repeated using a high permittivity dielectric pad positioned laterally on the phantom to validate simulations thereof. The dielectric pad was constructed using a deuterated suspension of barium titanate resulting in a relative permittivity of 286 and an electrical conductivity of 0.44 S/m, and measured 14 × 14 cm in size and 1 cm in thickness (37).

Results

Phantom design

The importance of including a spherical air cavity within the otherwise homogeneous phantom is illustrated in Figure 2, which compares simulated B_1^+ fields in the heterogeneous head model, a head model with homogeneous dielectric properties, and the ellipsoidal phantom without and with the spherical air cavity in place. Some specific local features of the B_1^+ patterns obtained in the heterogeneous head model are different from those obtained in the homogeneous head model, such as the pronounced left-right asymmetry produced only in the heterogeneous head model. This asymmetry is also absent in the homogeneous ellipsoidal phantom without spherical cavity. By including the air cavity (illustrated as a dashed circle) in the phantom, the correspondence with the B_1^+ distribution obtained in the heterogeneous head model is much better.

Static and RF field mapping

Figure 3 shows experimental B_0 and B_1^+ maps obtained in vivo and in the phantom using the commercial RF coil, illustrating a strong similarity between them. Both the B_0 as well as the B_1^+ perturbations induced by the nasal cavity are accurately reproduced by the spherical air cavity in the phantom. In addition, the agreement in absolute RF transmit efficiency indicates that the phantom presents a realistic load to the RF coil.

Figure 4 shows a comparison between simulated and measured B_1^+ maps using the custom-built birdcage. Both the absolute transmit efficiency as well as the relative B_1^+ distributions show a compelling agreement, with the simulation yielding a peak efficiency of 0.71 μT/√W compared to 0.72 μT/√W measured experimentally.

MR thermometry

Figure 5 compares the simulated and measured temperature difference maps obtained after 30 minutes of heating in the custom-built birdcage, which were validated using two fiber optic probes. The simulated data show a good agreement with measured data, with a peak temperature increase of 8.6 °C simulated compared to a 8.4 °C measured (both without dielectric pads). The root-mean-square errors between the fiber optic probe readings and MR thermometric data, calculated over the entire 30 minutes measurement period, were 0.13 °C and 0.18 °C for probetips #1 and #2, respectively.

Discussion

A simple head-sized phantom has been presented which allows realistic static and radiofrequency system characterization and provides a useful tool for methodological development of neuroimaging at high fields. The phantom produces realistic B_0 and B_1^+ nonuniformities similar to those encountered in the human head, and allows for accurate MR thermometry measurements for RF validation purposes. The simplicity and symmetry of the design, as opposed to taking an irregular head shaped shell, not only allows for easy and economical production, but also allows for easy interpretation of physical mechanisms to better direct modeling efforts. This makes the phantom a strong candidate as a reference phantom for high field MRI, where RF safety evaluation is becoming more important and methodological development more demanding.

A spherical air cavity was introduced in the phantom as this was found to be an important contributor to the B_1^+ asymmetries observed in vivo (30). These asymmetric features were also observed in other studies at our institute, and required an asymmetric and gender-specific B_1^+ correction method to (38) to take into account the typically larger nasal cavity in men (38). Although this was not the goal of the current phantom design, future developments towards a gender-specific phantom may consider this aspect.

In addition to yielding more realistic RF field distributions, the spherical cavity also reproduces the local B_0 inhomogeneities typically encountered in the frontal lobes. The joint-correspondence of these field nonuniformities can be of great interest in the area of spatiotemporal RF pulse design where both B_1^+ variations as well as off-resonance behavior have to be accounted for. Some smaller B_0 inhomogeneities measured around the ear canals in vivo were not reproduced in the phantom, as can be observed from Fig. 2a, as these anatomical features were not included in the design, but can be incorporated without much modification.

Advantages of the demonstrated RF validation procedure compared to other approaches such as using near field probes (39,40) include the simplicity of the experiment as well as the realistic experimental conditions to which the RF coil is exposed. Methods using near-field probes typically require a mechanical positioning system to scan the interior of the phantom, which is difficult to realize within the MR scanner and in ellipsoidal phantom designs. Performing the RF validation via MR thermometry allows for arbitrary phantom geometries and ensures that the RF coil will be exposed to similar RF coupling mechanisms as those of the corresponding in vivo scenario.

The current study focused on evaluating the phantom in a neuroimaging setup at a field strength of 7T, but the approach can essentially be transferred to any field strength. Although the 7T birdcage head coil was used to guide the phantom design, additional studies confirmed that the phantom also produces realistic B_1^+ fields in a 16-channel transmit array for 9.4T ((41); data provided as supplementary material). We do note that, as the phantom does not incorporate a torso section, the RF field response within a body-sized RF transmit coil with larger longitudinal field-of-view may be substantially different from the in vivo situation.

Residual minor differences between RF modeling and experimental characterization may arise from various sources, such as residual cable coupling effects, manufacturing tolerances on capacitor values, errors in phantom positioning within the RF coil, or the presence of the plexiglas support structure and oil phantoms which were not taken into account in the simulations. Another source of experimental error is the limited dynamic range of the B_1^+ mapping sequence, especially in areas of lower transmit efficiency, which can be improved by employing B_1^+ mapping sequences with a higher dynamic range (42).

A limitation of the simplified two-compartment phantom design is that the impact of tissue heterogeneities on local RF heating cannot be captured. For this purpose, multi-compartment designs would be desirable, however these are difficult to implement (23). Finally we note that, although the phantom has been shown to be suitable for guiding the validation of simulated RF coils, the measured temperature increases should not be taken as a surrogate measure for in vivo tissue heating, which requires heterogeneous body models as well as the incorporation of thermoregulatory response mechanisms (15).

Acknowledgement

The authors are grateful to Dr. Leoor Alon, Dr. Sukhoon Oh and Thomas Ruytenberg for helpful discussions related to the MR thermometry experiments, Dr. Oliver Kraff and Carlotta Ianniello for discussions on PVP and Jiying Dai for assistance in filling the phantom. This work was funded by the Nederlandse Organisatie voor Wetenschappelijk Onderzoek (NWO), STW Project #13375.

References

1. Yoshimura K, Kato H, Kuroda M, et al. Development of a tissue-equivalent MRI phantom using carrageenan gel. Magn Reson Med 2003;50:1011–1017. doi: 10.1002/mrm.10619.

2. Kato H, Kuroda M, Yoshimura K, Yoshida A, Hanamoto K, Kawasaki S, Shibuya K, Kanazawa S. Composition of MRI phantom equivalent to human tissues. Med Phys 2005;32:3199–3208. doi: 10.1118/1.2047807.

3. Shmueli K, Thomas DL, Ordidge RJ. Design, construction and evaluation of an anthropomorphic head phantom with realistic susceptibility artifacts. J Magn Reson Imaging 2007;26:202–207. doi: 10.1002/jmri.20993.

4. Hellerbach A, Schuster V, Jansen A, Sommer J. MRI Phantoms – Are There Alternatives to Agar? Oreja-Guevara C, editor. PLoS One 2013;8:e70343. doi: 10.1371/journal.pone.0070343.

5. Cho GY, Kim S, Jensen JH, Storey P, Sodickson DK, Sigmund EE. A versatile flow phantom for intravoxel incoherent motion MRI. Magn Reson Med 2012;67:1710–1720. doi: 10.1002/mrm.23193.

6. Yang QX, Wang J, Collins CM, Smith MB, Zhang X, Ugurbil K, Chen W. Phantom design method for high-field MRI human systems. Magn Reson Med 2004;52:1016–1020. doi: 10.1002/mrm.20245.

7. ASTM F2182 - 11a, “Standard Test Method for Measurement of Radio Frequency Induced Heating On or Near Passive Implants During Magnetic Resonance Imaging”, ASTM International. doi: 10.1520/F2182-11A.

8. Ugurbil K. Magnetic resonance imaging at ultrahigh fields. IEEE Trans Biomed Eng 2014;61:1364–79. doi: 10.1109/TBME.2014.2313619.

9. Hoult DI. Sensitivity and Power Deposition in a High-Field Imaging Experiment. J Magn Reson Imaging 2000;12:46–67.

10. Collins CM, Liu W, Schreiber W, Yang QX, Smith MB. Central brightening due to constructive interference with, without, and despite dielectric resonance. J Magn Reson Imaging 2005;21:192–196. doi: 10.1002/jmri.20245.

11. Sled JG, Pike GB. Standing-wave and RF penetration artifacts caused by elliptic geometry: an electrodynamic analysis of MRI. IEEE Trans Med Imaging 1998;17:653–662. doi: 10.1109/42.730409.

12. Brink WM, Börnert P, Nehrke K, Webb AG. Ventricular B1+ perturbation at 7 T - real effect or measurement artifact? NMR Biomed 2014;27:617–620. doi: 10.1002/nbm.3112.

13. Davis PL, Shang C, Talagala L, Pasculle AW. Magnetic resonance imaging can cause focal heating in a nonuniform phantom. IEEE Trans Biomed Eng 1993;40:1324–1327. doi: 10.1109/10.250588.

14. Collins CM, Li S, Smith MB. SAR and B1 field distributions in a heterogeneous human head model within a birdcage coil. Magn Reson Med 1998;40:847–856.

15. Alon L, Deniz CM, Carluccio G, Brown R, Sodickson DK, Collins CM. Effects of anatomical differences on electromagnetic fields, SAR, and temperature change. Concepts Magn Reson Part B Magn Reson Eng 2016;46:8–18. doi: 10.1002/cmr.b.21317.

16. Hoffmann J, Henning A, Giapitzakis IA, Scheffler K, Shajan G, Pohmann R, Avdievich NI. Safety testing and operational procedures for self-developed radiofrequency coils. NMR Biomed 2016;29:1131–1144. doi: 10.1002/nbm.3290.

17. Katscher U, Börnert P, Leussler C, van den Brink JS. Transmit SENSE. Magn Reson Med 2003;49:144–150.

18. Yip CY, Fessler JA, Noll DC. Iterative RF pulse design for multidimensional, small-tip-angle selective excitation. Magn Reson Med 2005;54:908–917. doi: 10.1002/mrm.20631.

19. Webb AG. Dielectric materials in magnetic resonance. Concepts Magn Reson 2011;38A:48–84.

20. Mobashsher AT, Abbosh AM. Three-Dimensional Human Head Phantom With Realistic Electrical Properties and Anatomy. IEEE Antennas Wirel Propag Lett 2014;13:1401–1404. doi: 10.1109/LAWP.2014.2340409.

21. Graedel NN, Polimeni JR, Guerin B, Gagoski B, Wald LL. An anatomically realistic temperature phantom for radiofrequency heating measurements. Magn Reson Med 2015;73:442–450. doi: 10.1002/mrm.25123.

22. Neves AL, Leroi L, Cochinaire N, Abdeddaim R, Sabouroux P, Vignaud A. Mimicking the Electromagnetic Distribution in the Human Brain: A Multi-frequency MRI Head Phantom. Appl Magn Reson 2017;48:213–226. doi: 10.1007/s00723-017-0862-4.

23. Wood S, Krishnamurthy N, Santini T, Raval S, Farhat N, Holmes JA, Ibrahim TS. Design and fabrication of a realistic anthropomorphic heterogeneous head phantom for MR purposes Lundberg P, editor. PLoS One 2017;12:e0183168. doi: 10.1371/journal.pone.0183168.

24. Ito K, Furuya K, Okano Y, Hamada L. Development and characteristics of a biological tissue-equivalent phantom for microwaves. Electron Commun Japan (Part I Commun 2001;84:67–77. doi: 10.1002/1520-6424(200104)84:4<67::AID-ECJA8>3.0.CO;2-D.

25. Duan Q, Duyn JH, Gudino N, de Zwart JA, van Gelderen P, Sodickson DK, Brown R. Characterization of a dielectric phantom for high-field magnetic resonance imaging applications. Med Phys 2014;41:102303. doi: 10.1118/1.4895823.

26. Park SM, Nyenhuis JA, Smith CD, et al. Gelled versus nongelled phantom material for measurement of MRI-induced temperature increases with bioimplants. IEEE Trans Magn 2003;39:3367–3371. doi: 10.1109/TMAG.2003.816259.

27. Ianniello C, de Zwart JA, Duan Q, Deniz CM, Alon L, Lee J-S, Lattanzi R, Brown R. Synthesized tissue-equivalent dielectric phantoms using salt and polyvinylpyrrolidone solutions. Magn Reson Med 2017. doi: 10.1002/mrm.27005.

28. Christ A, Kainz W, Hahn EG, et al. The Virtual Family—development of surface-based anatomical models of two adults and two children for dosimetric simulations. Phys Med Biol 2010;55:N23-38. doi: 10.1088/0031-9155/55/2/N01.

29. Gabriel S, Lau RW, Gabriel C. The dielectric properties of biological tissues: III. Parametric models for the dielectric spectrum of tissues. Phys Med Biol 1996;41:2271–93. doi: 10.1088/0031-9155/41/11/003.

30. Brink W, Webb A. Appearant B1+ Asymmetry in Symmetric Objects at High Fields. In: Proceedings of the 23rd Annual Meeting of ISMRM, Milan, Italy, 2014. p. 4815.

31. Sengwa RJ, Sankhla S. Chain length effect on dynamical structure of poly (vinyl pyrrolidone)-polar solvent mixtures in dilute solution of dioxane studied by microwave dielectric relaxation measurement. Pramana - J Phys 2006;67:375–381. doi: 10.1007/s12043-006-0083-0.

32. Mcintosh RL, Anderson V. A Comprehensive Tissue Properties Database Provided For The Thermal Assessment Of A Human At Rest. Biophys Rev Lett 2010;5:129–151. doi: 10.1142/S1793048010001184.

33. Wald LL, Wiggins GC, Potthast A, Wiggins CJ, Triantafyllou C. Design considerations and coil comparisons for 7 T brain imaging. Appl Magn Reson 2005;29:19–37. doi: 10.1007/BF03166954.

34. Roemer PB, Edelstein WA, Hayes CE, Souza SP, Mueller OM. The NMR phased array. Magn Reson Med 1990;16:192–225. doi: 10.1002/mrm.1910160203.

35. Poorter J De, Wagter C De, Deene Y De, Thomsen C, Ståhlberg F, Achten E. Noninvasive MRI Thermometry with the Proton Resonance Frequency (PRF) Method: In Vivo Results in Human Muscle. Magn Reson Med 1995;33:74–81. doi: 10.1002/mrm.1910330111.

36. Rieke V, Butts Pauly K. MR Thermometry. J Magn Reson Imaging 2008;27:376–90. doi: 10.1002/jmri.21265.

37. Teeuwisse WM, Brink WM, Haines KN, Webb AG. Simulations of high permittivity materials for 7 T neuroimaging and evaluation of a new barium titanate-based dielectric. Magn Reson Med 2012;67:912–918. doi: 10.1002/mrm.24176.

38. Samolinski BK, Grzanka A, Gotlib T. Changes in Nasal Cavity Dimensions in Children and Adults by Gender and Age. Laryngoscope 2007;117:1429–1433. doi: 10.1097/MLG.0b013e318064e837.

39. Bitz AK, Kraff O, Orzada S, Maderwald S, Brote I, Johst S, Ladd ME. Assessment of RF Safety of Tx Coils at 7 Tesla by Experimental and Numerical Procedures. In: Proceedings of the 19th Annual Meeting ISMRM, Montreal, QC, Canada, 2011. p. 490.

40. Saniour I, Gaborit G, Perrier A-L, Gillette L, Revillod G, Sablong R, Duvillaret L, Beuf O. Electro-optic probe for real-time assessments of RF electric field produced in an MRI scanner: Feasibility tests at 3 and 4.7 T. NMR Biomed 2017:e3849. doi: 10.1002/nbm.3849.

41. Shajan G, Kozlov M, Hoffmann J, Turner R, Scheffler K, Pohmann R. A 16-channel dual-row transmit array in combination with a 31-element receive array for human brain imaging at 9.4 T. Magn Reson Med 2014;71:870–879. doi: 10.1002/mrm.24726.

42. Padormo F, Beqiri A, Malik SJ, Hajnal J V. PRIMO: Precise radiofrequency inference from multiple observations. Magn Reson Med 2015;74:372–83. doi: 10.1002/mrm.25404.

Figures

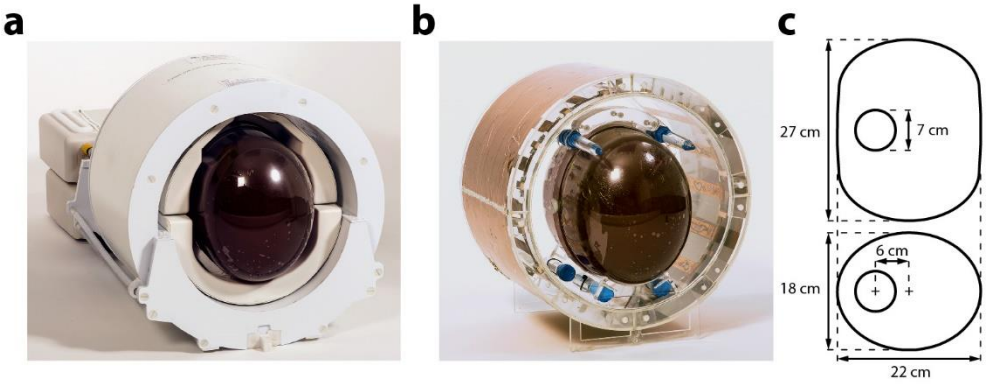

Figure 1. Illustrations of the experimental setup and phantom design. Shown are the head-sized phantom in the commercial 7T neuroimaging setup (a), custom-built birdcage coil used for the RF validation study (b) and schematic drawings of the proposed phantom in a sagittal (top) and transverse (bottom) view (c).

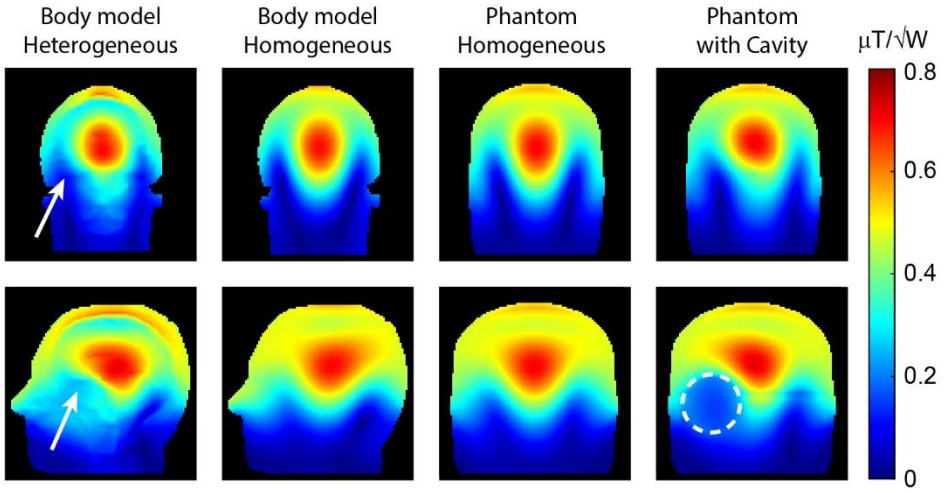

Figure 2. Simulated effect of different phantom approximations on the B_1^+ field, shown in coronal (top) and sagittal (bottom) cross-sections. The asymmetric features in the B_1^+ patterns observed in the heterogeneous head model (indicated by the arrows) are only reproduced when the spherical cavity is incorporated into the phantom (dashed circle).

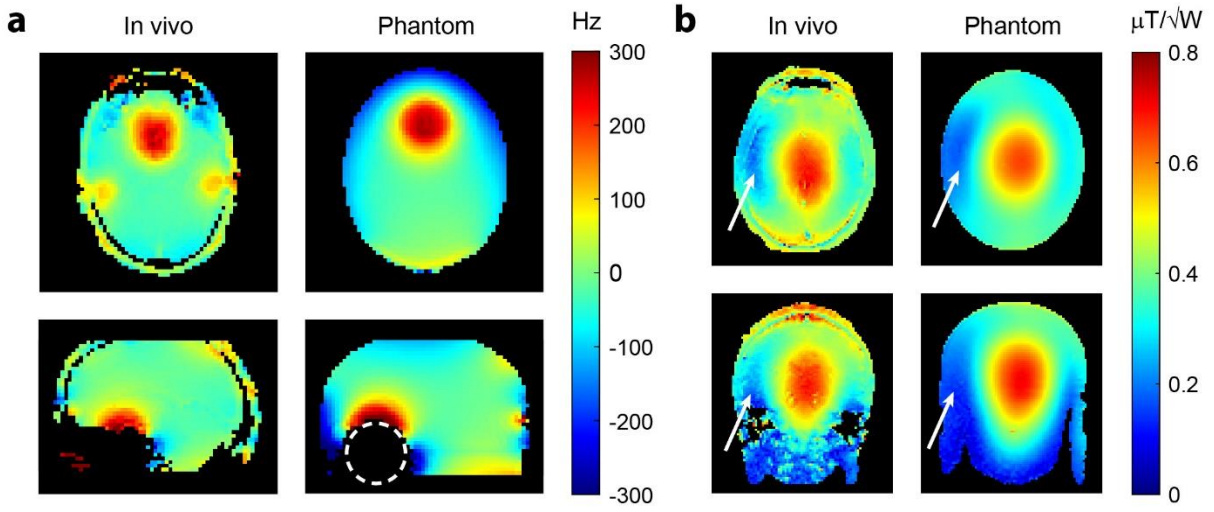

Figure 3. B_0 and B_1^+ field characterization in the phantom and in vivo using the commercial RF coil setup. Both the static (a) and RF transmit (b) fields are in good correspondence with in vivo measurements. B_1^+ field data is normalized to coil input power.

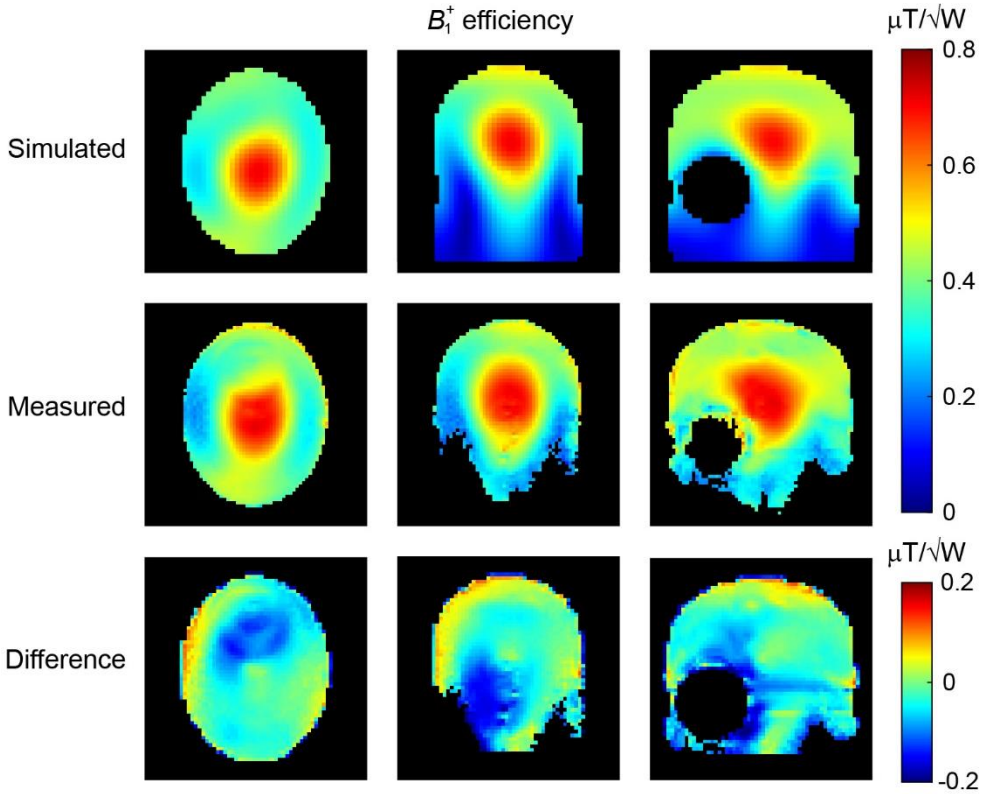

Figure 4. B_1^+ validation results. Shown are the simulated (top) and measured (middle) B_1^+ fields in the custom-built birdcage coil, and their difference (simulated – measured; bottom) in three orthogonal views (left-right). Both the absolute transmit efficiency as well as the relative B_1^+ distributions show a compelling agreement, with the peak efficiency agreeing within 0.02 μT/√W.

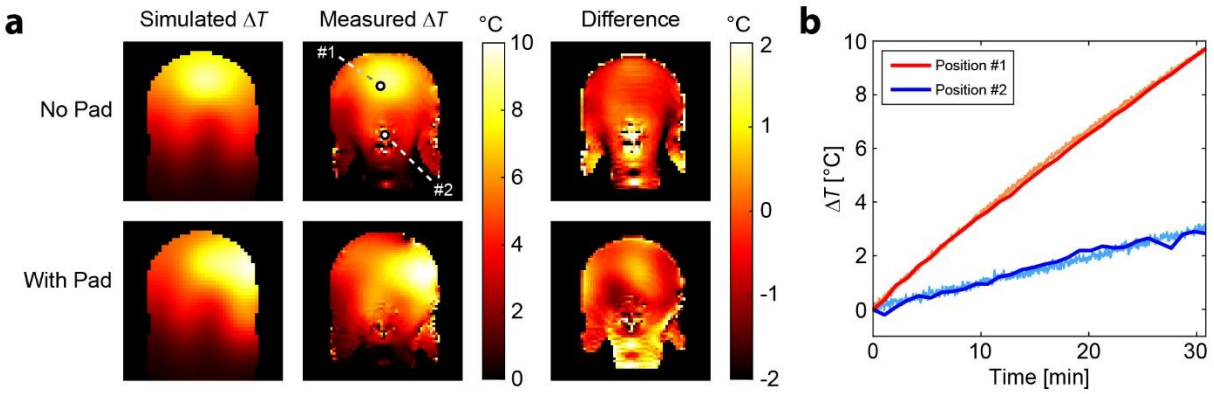

Figure 5. Thermometric validation results. Shown are coronal maps (a) comparing the simulated temperature increase (left) with measurements (middle) showing good correspondence as indicated by their difference (simulated – measured; right), both without (top) and with (bottom) a high permittivity dielectric pad. Validation of the MR thermometry results using two fiber optic probes (b) confirms the validity of the data, with root-mean-square errors between of 0.13 °C and 0.18 °C for probetips #1 and #2, respectively. The locations of the probes are indicated by the circles in (a).

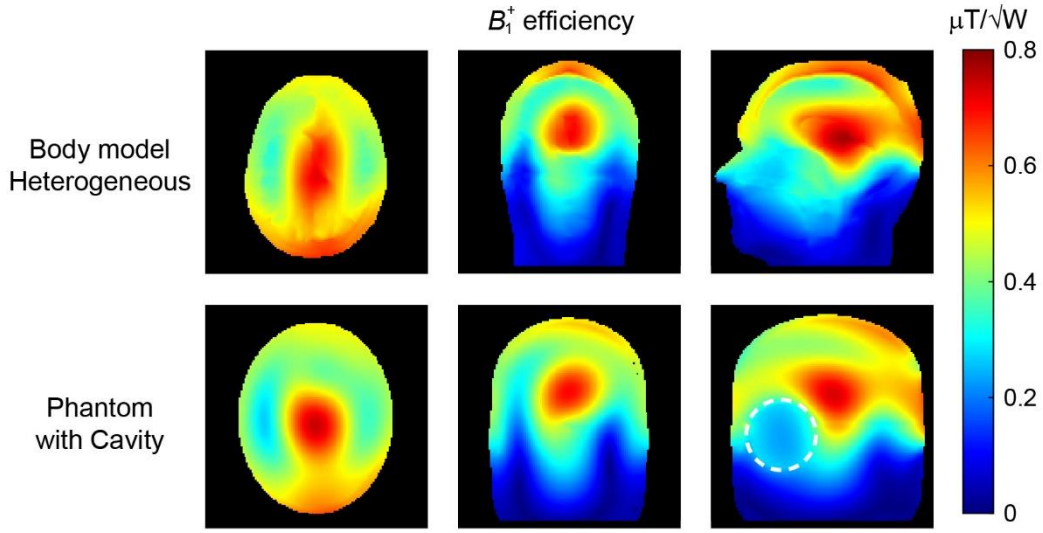

Supplementary Figure S1. Simulated comparison of B_1^+ fields obtained in the heterogeneous head model and the proposed phantom using a 16-channel transmit array for 9.4T (41).